Monthly Notices
of the
ROYAL ASTRONOMICAL SOCIETY

MNRAS **478,** 3513–3524 (2018) doi:10.1093/mnras/sty1468

Intra-day optical multi-band quasi-simultaneous observation of BL Lacertae object S5 0716+714 from 2013 to 2016

Xiaoyuan Zhang, Jianghua Wu★ and Nankun Meng

Department of Astronomy, Beijing Normal University, Beijing 100875, China

Accepted 2018 June 4. Received 2018 June 4; in original form 2018 February 14

ABSTRACT

We performed quasi-simultaneous optical multi-band monitoring of the BL Lac object S5 0716+714 on seven nights from 2013 to 2016. Intra-day variability was found on all seven nights. The source was faintest on JD 245 6322 with 14.15 mag and brightest on JD 245 7437 with 12.51 mag in the *R* band. The maximum intra-day variation that we observed was 0.15 mag in the *B* band on JD 245 6322. Both bluer-when-brighter and achromatic spectral behaviours were observed on the intra-day timescale. On the longer-term scale, the object exhibited mild bluer-when-brighter behaviour between the *B* and *R* bands. We estimate the inter-band lags using two independent methods. The variation in the *B* band was observed to lag behind that in the *I* band by about 15 min on JD 245 7315. We compare this lag with one reported previously and discuss the origin of these lags.

Key words: galaxies: active – BL Lacertae objects: individual: S5 0716+714 – galaxies: photometry.

1 INTRODUCTION

Blazars are a subset of active galactic nuclei (AGNs). They are those AGNs with their relativistic jets pointing at a small angle to our line of sight (Urry & Padovani 1995). Blazars can be classified into BL Lacertae objects and flat-spectrum radio quasars (FSRQs) according to the strength of their emission lines. BL Lac objects have absent or weak emission lines (EW $\leq$ 5 Å), while FSRQs show strong emission lines in their spectra. In general, there are two humps in the spectral energy distribution (SED) of blazars. The first hump, extending from radio to UV or soft X-ray, is likely dominated by synchrotron radiation from the relativistic jet, and the second, covering UV or soft X-ray to γ-ray, dominated by inverse Compton emission. According to the frequency of the synchrotron peak, blazars are classified as low synchrotron-peaked blazars (LSP, $\nu_{\rm syn\_peak} \leq 10^{14}$ Hz), intermediate synchrotron-peaked blazars (ISP, $10^{14} < \nu_{\rm syn_peak} < 10^{15}$Hz) and high synchrotron-peaked blazars (HSP, $\nu_{\rm syn_peak} \geq 10^{15}$Hz). The most striking characteristic of blazars is their dramatic variability from radio to γ-ray (e.g. Böttcher et al. 2003; Raiteri et al. 2008; Villata et al. 2009). The variability timescales vary from minutes to years. Rapid variability with timescales less than one day is called intra-day variability (IDV). Short-variation timescales limit the emission regions within extremely small sizes. Studying the optical intra-day variability can help to constrain the physical processes at the base of the blazar jets, e.g. the particle acceleration and cooling mechanism, magnetic field geometry, plasma instability in the jet etc. Previous studies of blazar optical IDV have made great progress since the first optical IDV was discovered by Miller, Carini & Goodrich (1989) in BL Lacertae. A systematic optical IDV search was performed by Heidt & Wagner (1996), where IDV was detected in 28 out of 34 1 Jy catalogue BL Lac objects. Gupta & Joshi (2005) reported that the probability of IDV detection is 80 to 85 per cent if the blazar is continuously observed over six hours. Most of the IDV-detected blazars are LSPs and ISPs (e.g. Gupta et al. 2008; Gaur et al. 2012c), whereas HSPs show little evidence of IDV (e.g. Gaur, Gupta & Wiita 2012a; Gaur et al. 2012b). Recently, Gupta (2018) has reviewed multi-wavelength IDV of blazars.

S5 0716+714 (RA $7^{\rm h}21^{\rm min}53^{\rm s}.45$, Dec. $71^{\rm o}20'36''.36$, J2000), one of the brightest BL Lac objects in the northern sky, is classified as an ISP according to its synchrotron-peak frequency of $10^{14.6}$ Hz (Abdo et al. 2010). The redshift is $z = 0.31 \pm 0.08$, estimated by Nilsson et al. (2008) by using the host galaxy as a 'standard candle', and later limited by Danforth et al. (2013) as $z < 0.322$. It is also one of the best-studied blazars with high variability from radio to γ-ray (e.g. Villata et al. 2008; Rani et al. 2013; Liao et al. 2014). In the optical regime, it exhibits fast variability with a duty cycle approximate to 1 (Wagner et al. 1996). A number of campaigns have been performed to study the IDV properties of this source (e.g. Villata et al. 2000; Raiteri et al. 2003; Nesci et al. 2005; Wu et al. 2005, 2007, 2012; Carini, Walters & Hopper 2011; Dai et al. 2013; Hu et al. 2014; Agarwal et al. 2016; Hong, Xiong & Bai 2017; Liu et al. 2017). Montagni et al. (2006) studied monitoring data on 102 nights from 1996 to 2003. The distribution of variability timescales followed an exponential law and the shortest timescale is about two hours. 72 hours Whole Earth Blazar Telescope (WEBT)

★ E-mail: jhwu@bnu.edu.cn

Table 1. Parameters of telescopes and terminal instruments.

Telescope	2.16 m	85 cm		80 cm	60 cm
		Old CCD	New CCD (after 2014)		
Optical design	Ritchey–Chrétien	Prime focus		Cassegrain	Prime focus
Focus ratio	f/9	f/3.3		f/10	f/4.23
CCD model	E2V 55-30	PI 1024 EBFT-1	Andor	PI 1300B	E2V 47-10
CCD size	1242 × 1152	1024 × 1024	2048 × 2048	1340 × 1300	512 × 512
Pixel scale (arcsec pixel^{-1})	0.457	0.96	0.96	0.52	1.95
FOV (arcmin^2)	9.46 × 8.77	16.4 × 16.4	32.8 × 32.8	11.5 × 11.2	16.6 × 16.6

Table 2. Details of observations.

Date	Julian date	Filter	Duration (h)	Temporal resolution (s)	Telescope	Good data ratio
2013 Jan. 29	245 6322	*B*	5.67	67.8	2.16 m	0.78
		R	5.50	119.0	80 cm	0.81
		I	5.33	23.0	85 cm	0.72
2015 Oct. 16	245 7312	*R*	3.51	50.0	80 cm	0.98
		I	3.39	45.6	60 cm	1.00
2015 Oct. 17	245 7313	*B*	3.18	200.2	80 cm	0.71
		V	3.12	10.0	85 cm	0.86
		R	3.17	199.3	80 cm	0.60
2015 Oct. 18	245 7314	*B*	2.64	35.0	85 cm	1.00
		R	2.79	50.0	80 cm	0.99
		I	2.72	45.6	60 cm	0.91
2015 Oct. 19	245 7315	*B*	3.12	25.2	85 cm	0.99
		R	3.23	34.0	80 cm	0.79
		I	3.40	25.4	60 cm	1.00
2016 Feb. 17	245 7436	*B*	9.17	103.1	85 cm	1.00
		V	9.15	103.1	85 cm	1.00
		R	9.21	103.1	85 cm	0.99
2016 Feb. 18	245 7437	*B*	4.95	91.1	85 cm	0.74
		V	4.92	91.1	85 cm	0.82
		R	4.95	91.1	85 cm	0.80

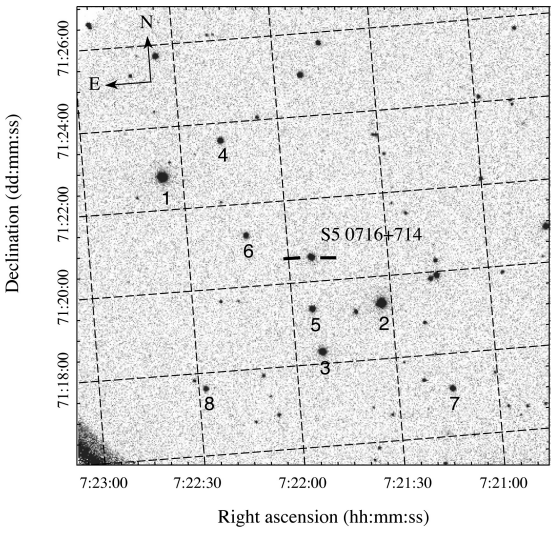

Figure 1. Finding chart of S5 0716+714 in the *R* band.

continuous observations show that the power spectrum density of the light curve is well fitted by $1/f^2$ power law, indicating the stochastic nature of the IDV (Bhatta et al. 2013). Meanwhile, quasi-periodic oscillations are occasionally reported (e.g. Wu et al. 2005; Rani et al. 2010b; Bhatta et al. 2016; Man et al. 2016; Hong, Xiong & Bai 2018).

During flares, spectral hystereses or time lags between two light curves at different wavelengths are sometimes observed. Most of these events are soft lags, i.e. variations at short wavelength lead those at long wavelength (e.g. Takahashi et al. 1996; Kataoka et al. 2000). On the other hand, hard lags are were also observed in a few cases (e.g. Fossati et al. 2000b). Different spectral hysteresis patterns as well as the position of the observation frequency relative to the synchrotron-peak frequency are essential to constrain different jet models, e.g. homogeneous single-zone leptonic models (Dermer 1998; Chiaberge & Ghisellini 1999) and the internal-shock model (Spada et al. 2001; Böttcher & Dermer 2010). For S5 0716+714, time lags among different electromagnetic wave regimes are frequently detected. Raiteri et al. (2003) reported that the radio flux variations at lower frequencies lagged the higher-frequency ones with time delays from a few days to weeks; Rani et al. (2013) stated that the optical/GeV flux variations lead the radio variability by ∼65 days. In the optical regime, inter-band lags have been reported by several authors. For example, Qian, Tao & Fan (2000) reported a six-minute lag between variations in the *V* and *I* bands; Villata et al. (2000) found a 10-min lag between the *B* and *I* bands; a plausible 11-min lag between the *B* and *I* bands was observed by Poon, Fan & Fu (2009); recently, Wu et al. (2012) reported a 30-min lag between the B' and R' bands; and later Man et al. (2016) observed a possible 1.5-min lag between the *B* and *I* bands. Since some of the time lags

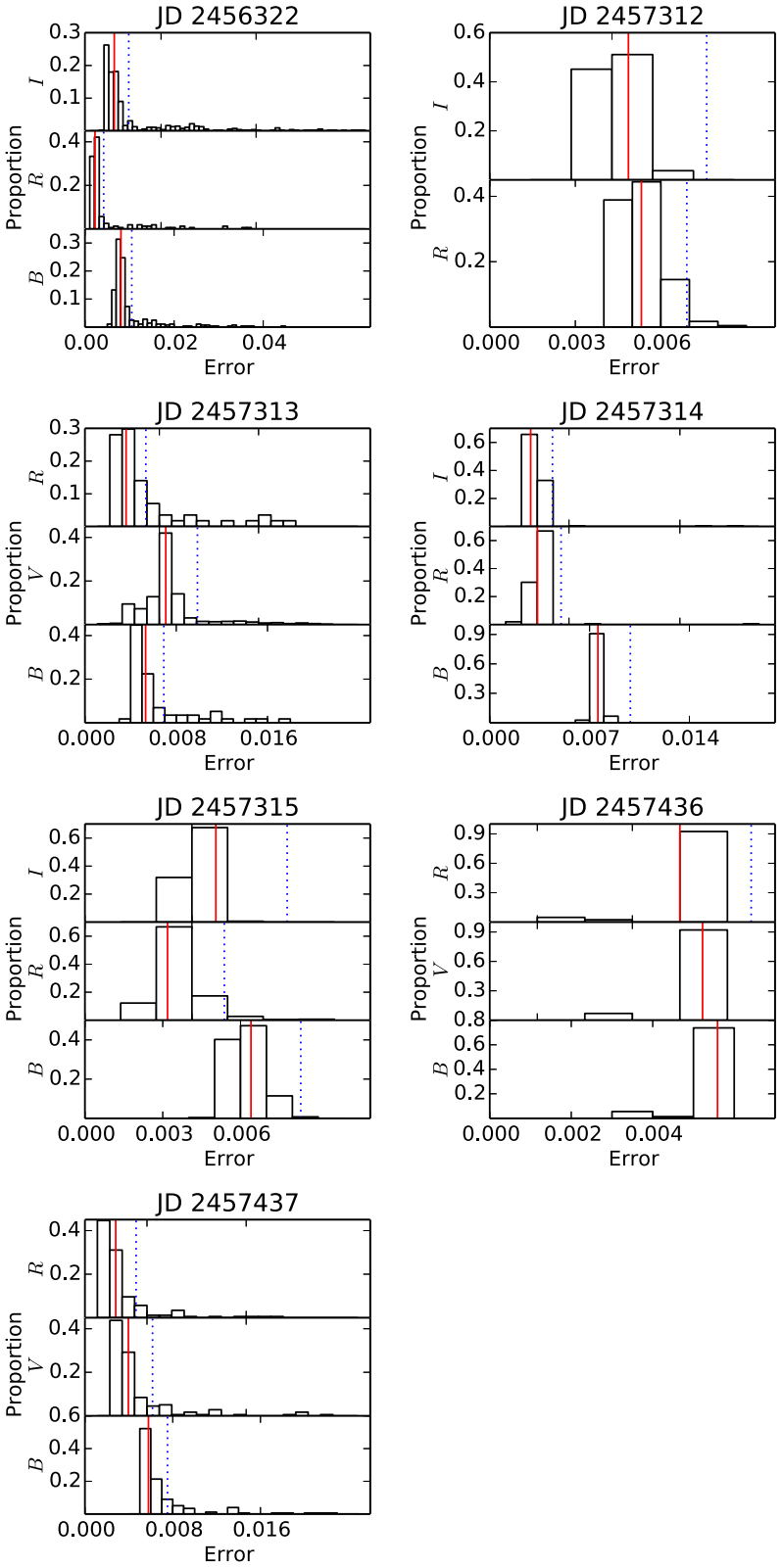

Figure 2. Photometry error distributions of each band on each night. Red solid lines represent the median value of errors and blue dotted lines represent 1.3 times the median value.

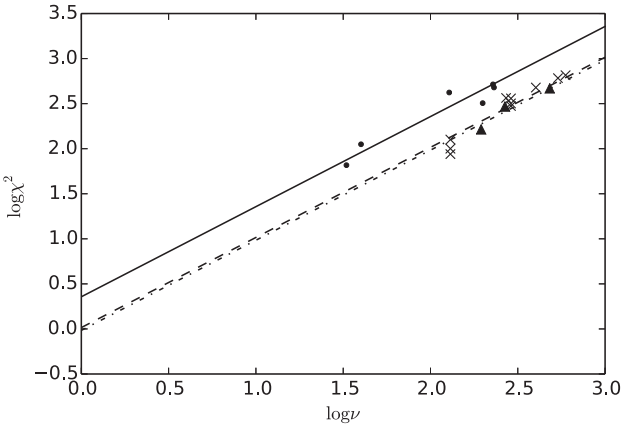

Figure 3. Regression with log χ^2 and log ν for each telescope. The crosses, dots and triangles represent data from the 85 cm, 80 cm and 60 cm telescopes, respectively. The dashed, solid and dash-dotted lines represent the fitting curves for the 85 cm, 80 cm and 60 cm telescopes, respectively.

are as short as only a few minutes, high temporal resolutions are needed to increase the probability of lag detection. Therefore, we performed multi-band quasi-simultaneous observations with high temporal resolutions. In this paper, we report our observation and analysis results.

This paper is organized as follows: In Section 2, we report details of observation and data reduction. In Section 3, we show the results of various analyses of our data including the IDV test, colour behaviour and cross-correlation analysis. The discussion and conclusion are given in Section 4 and 5.

2 OBSERVATION AND DATA REDUCTION

2.1 Telescopes and observation strategy

Usually, the temporal resolution of quasi-simultaneous observations by one telescope equipped with multiple filters is limited by the number of filters, because exposures with different filters are taken in a cyclic pattern. Wu et al. (2007) utilized an objective prism and a multi-peak interference filter to achieve exactly simultaneous observations at three passbands. However, this method may introduce some extra uncertainties when adopting an elongated aperture in photometry. Also, this method does not work well with a crowded stellar field. As a result, we adopted a compromise, using multiple telescopes to monitor the object with different filters independently. This allows us to obtain high temporal resolution light curves in all bands; see Man et al. (2016) for an example.

During our observations, four telescopes at Xinglong Observatory, National Astronomical Observatories, Chinese Academy of Science (NAOC) were used. The parameters of these telescopes are listed in Table 1. The computer clocks of these telescopes were synchronized by the GPS clock. Observations were performed on seven nights from 2013 to 2016. On 2013 January 29 (JD 245 6322), the 2.16 m, 85 cm and 80 cm telescopes were selected for observation. From 2015 October 16–19 (JD 245 7312 to JD 245 7315), the 60 cm, 80 cm, 85 cm telescopes were selected. From 2016 February 17–18 (JD 245 7436 to JD 245 7437), only the 85 cm telescope was used. Details of filters, observation durations, and temporal resolutions are listed in columns 3–5 of Table 2.

2.2 Data reduction

For original data obtained in each session, we follow the standard process including bias-subtraction and flat-fielding with IRAF.[1] To find the best aperture radius, first, we set it as 1.5, 2.0, 2.5, 3.0, 3.5 and 4.0 times the full width at half-maximum (FWHM) of the stellar images. The inner and outer radii of the sky annuli are 7 and 9 times the FWHM. Then the instrument magnitudes of S5 0716+714 and stars 1 to 8 in the finding chart (see Fig. 1) are extracted from the frames. In order to minimize the intrinsic error of differential magnitudes, the comparison stars should be somewhat brighter than the object (Howell, Mitchell & Warnock 1988). As a result, two bright unsaturated stars 2 and 3 are selected as comparison stars and star 5 as the check star. We adopt the aperture with the smallest standard deviation of differential magnitude (the difference between instrumental magnitudes of two reference stars). The magnitude of S5 0716+714 is calibrated relative to those of stars 2 and 3. The differential magnitude of the check star (the difference between instrumental magnitudes of the check star and the average value of two comparison stars) is also derived to ensure photometric accuracy. Standard magnitudes of all comparison stars are given by Villata et al. (1998) in the *B*, *V*, *R* bands and by Ghisellini et al. (1997) in the *I* band.

We calculated the distributions of the raw photometric errors on each night. The results are plotted in Fig. 2. Here, the red solid and blue dotted lines represent 1 and 1.3 times the median values of the raw photometric errors of each light curve, respectively. Errors in tails on the right-hand side can be caused by sudden changes of weather conditions and brightening of the skylight at dawn. We empirically adopt a threshold of 1.3 times the median value of the errors and exclude those data with errors larger than the threshold. The good data ratio of each light curve is listed in column 7 of Table 2.

2.3 Error scaling

The photometric error yielded by APPHOT in IRAF is believed to be underestimated. Hence, a factor η is introduced to amplify the underestimated error. Different values were calculated by different authors, e.g. 1.3 by Bachev, Strigachev & Semkov (2005), 1.5 by Stalin et al. (2004), Gopal-Krishna et al. (2003), and 1.73 by Garcia et al. (1999), etc.

Before subsequent analysis, we should estimate the scale factor η for each telescope. The method of Goyal et al. (2013) is adopted. First, for each light curve, we calculate the χ^2 value of differential magnitudes of the check star by using the following equation:

$$\chi^2 = \sum_{i=1}^{N} \frac{(V_i - \overline{V})^2}{\sigma_i^2}, \tag{1}$$

where V_i is the ith differential magnitude, $\overline{V}$ is the mean of all differential magnitudes, and σ_i is the error of V_i, which is propagated from raw photometry errors of stars. The corresponding degree of freedom is

$$\nu = N - 1 = \sum_{i=1}^{N} \frac{(V_i - \overline{V})^2}{\eta^2 \sigma_i^2} = \chi^2/\eta^2. \tag{2}$$

[1] IRAF is distributed by the National Optical Astronomy Observatories, which are operated by the Association of Universities for Research in Astronomy, Inc., under cooperative agreement with the National Science Foundation.

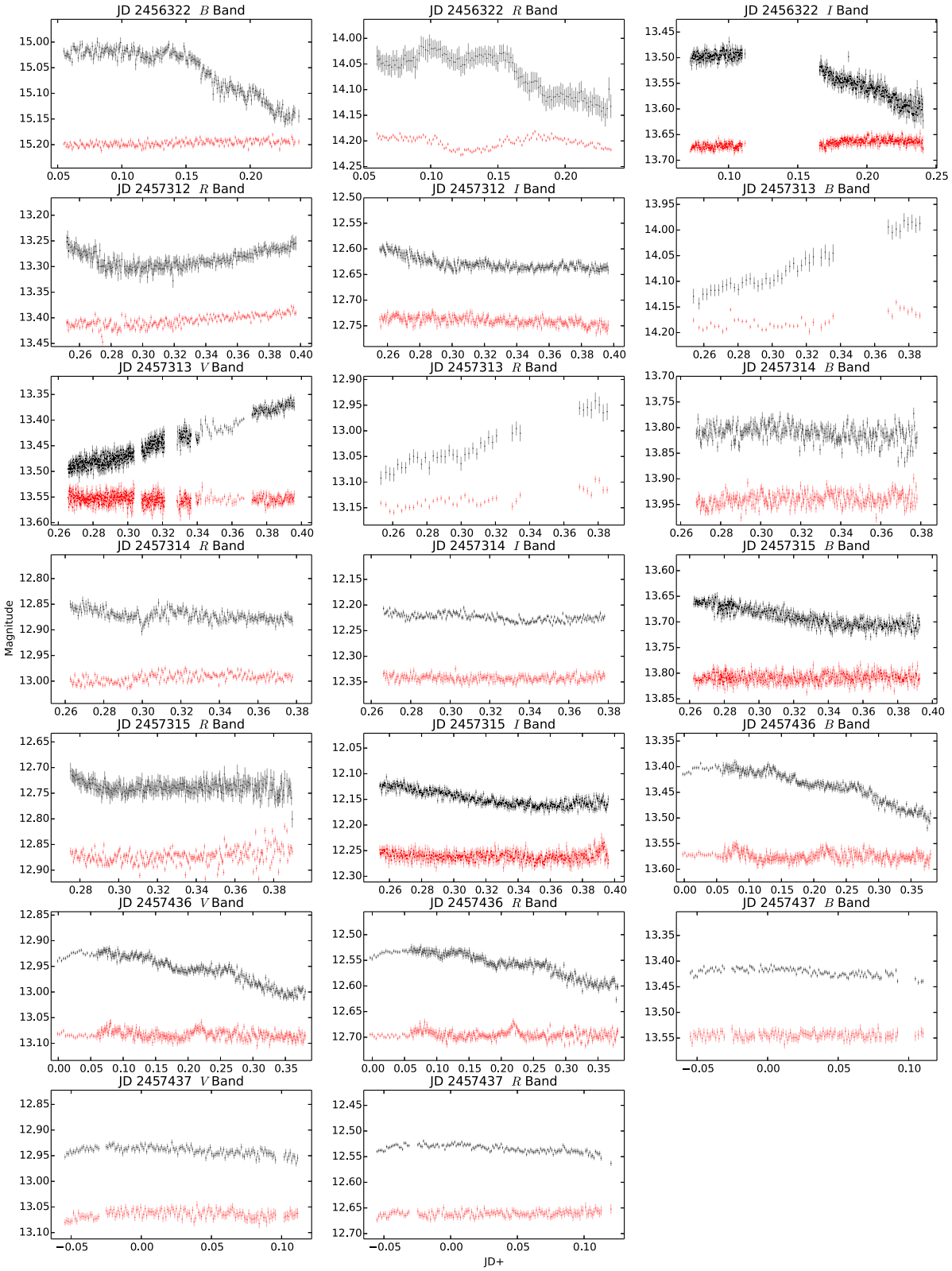

Figure 4. Intra-day light curves in each band on each day. The light curves of the check star are plotted in red dots and shifted to a proper position under the source's light curves.

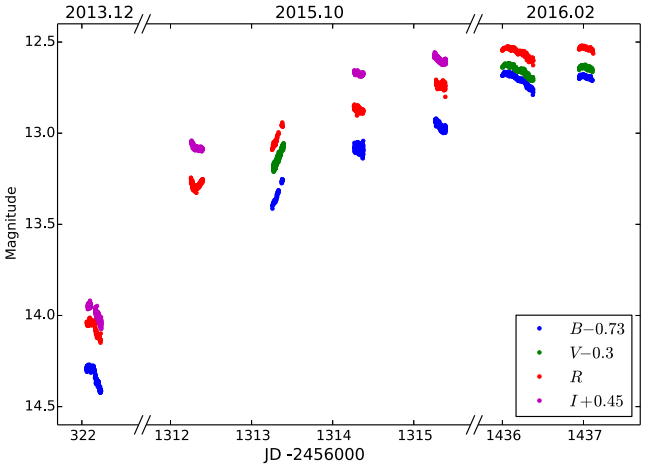

Figure 5. Overall multi-band light curves in seven days. Light curves in the *B*, *V* and *I* bands are shifted.

Then we perform a regression analysis with $\log \chi^2$ and $\log \nu$ with a fixed slope 1. The intercept K is obtained from

$$\log \chi^2 = K + \log \nu, \quad (3)$$

where $10^K = \eta^2$. We obtain $\eta = 1.02$ for the 85 cm telescope, $\eta = 1.51$ for the 80 cm telescope and $\eta = 0.98$ for the 60 cm telescope. The fitting lines are plotted in Fig. 3. Because there is only one light curve for the 2.16 m telescope and the 85 cm telescope with old CCD, we use reduced χ^2 values to represent η^2. The η values for the 2.16 m telescope and the 85 cm telescope with old CCD are 1.28 and 1.20, respectively. In the next section, our analysis is based on the error-scaled data.

It is clear that the scale factors of the 85 cm telescope and the 60 cm telescope are much less than that of the 80 cm telescope. This offset may be caused by some unknown interference in the 80 cm telescope light path, which adds extra fluctuations after flat-fielding and amplifies the η factor. Also, this unknown interference could create pseudo flares in the light curves of the object.

3 RESULTS

3.1 Light curves

The intra-day light curves of the source are plotted in Fig. 4. The differential light curves of the check star are also plotted to indicate the photometric accuracy. The overall light curves in seven days are plotted in Fig. 5 to show the inter-day variability. During our observation, the source was faintest on JD 245 6322 with 14.15 mag in the *R* band and reached the brightest state on JD 245 7437 with 12.51 mag in the *R* band.

It is clear that the variations on JDs 245 6322, 245 7313 and 245 7436 are significant. On JD 245 6322, variation in the *B* band reaches 0.15 mag, and the maximum variation rate is 0.085 mag h^{-1}. On JD 245 7313, the source turned bright monotonously in all three bands with a variation rate of about 0.053 mag h^{-1}. On JD 245 7436, the light curves descend with a moderate rate and a plateau can be seen in all bands. On JDs 245 7314 and 245 7437, the source shows marginal intra-day variations in all bands. On JD 245 7315, the brightness descended and then rose again in the *B* and *I* bands. Inter-day variations are considerable. From JDs 245 7312 to 245 7315, the *R*-band magnitude varied by 0.56 mag within four days.

We notice that the check star's differential light curves observed by the 80 cm telescope are slightly unstable. This phenomenon is consistent with the large η value obtained in Section 2.3. The unknown interference in the 80 cm telescope affects the photometric accuracy. When the source has significant IDV, the influence tends to be relative low, e.g. light curves on JDs 245 6322 and 245 7313. However, when the source is only marginally variable, this influence could alter the entire profile of the light curve. On JDs 245 7312, 245 7314 and 245 7315, light curves in the *R* band are considerably different from those in other bands. The incongruity could produce pseudo results in colour variation and cross-correlation analyses. As a result, the *R*-band light curves on those three days should be ruled out from these two analyses.

3.2 IDV test

To quantitatively test the intra-day variability of the source, we adopt two up-to-date robust statistical tests. They are the enhanced *F*-test and the nested analysis of variance (ANOVA) (de Diego et al. 2015).

In the original *F*-test (de Diego 2010), the statistical value F is obtained from the variances in the differential magnitudes of the object and a check star. The enhanced *F*-test includes data from several field stars to produce a more robust result. In this test, we use the brightest unsaturated star 2 as a comparison star to get the differential magnitudes of the object and field stars 3 to 8. For stars 3 to 8, we perform the following procedures to get the stacked differential light curves. First, we fit the mean differential magnitudes and the corresponding standard deviations with an exponential curve. Then we scale the variance of each differential light curve to the same level of the object. Finally we subtract the mean value of each scaled differential light curve. The variance of the stacked differential light curves of field stars is calculated as the denominator of the F value. The F value, two corresponding degrees of freedom and the probability of passing the null hypothesis are listed in columns 3 to 6 in Table3.

In the nested ANOVA, multiple field stars are involved as comparison stars. In our test, stars 2 to 8 are used to calculate the differential light curves of the object. Then the seven differential light curves are divided into a number of groups with five points in each group. We follow equation (4) of de Diego et al. (2015) to test the null hypothesis that the deviation of the mean values of differential light curves in each group is zero. The statistical value F, two degrees of freedom and the probability of passing the null hypothesis are listed in columns 7 to 10 in Table 3. Meanwhile, in order to test the invariability of the check star, we also apply the test to star 5 and present the results in columns 11 to 14.

For most observation sessions, the light curves of the object pass both tests and the light curves of the check star fail to pass the nested ANOVA. So the object was variable in these sessions. In two observation sessions with the 80 cm telescope, the light curves of the object fail to pass the *F*-test, and the light curves of the check star pass the nested ANOVA. This kind of behaviour is caused by the unknown interference in the light path of the 80 cm telescope. The light curve of each object in the field is added with pseudo variations. We cannot determine the variability in these sessions. In another two sessions with the 80 cm telescope, for the same reason, the light curves of the check star pass the nested ANOVA, but the object's light curves pass both tests as well. We regard the object as variable. All abnormal behaviours observed by the 80 cm telescope are marked with *a*. In four sessions with other telescopes, the check star's light curves pass the nested ANOVA and are marked with

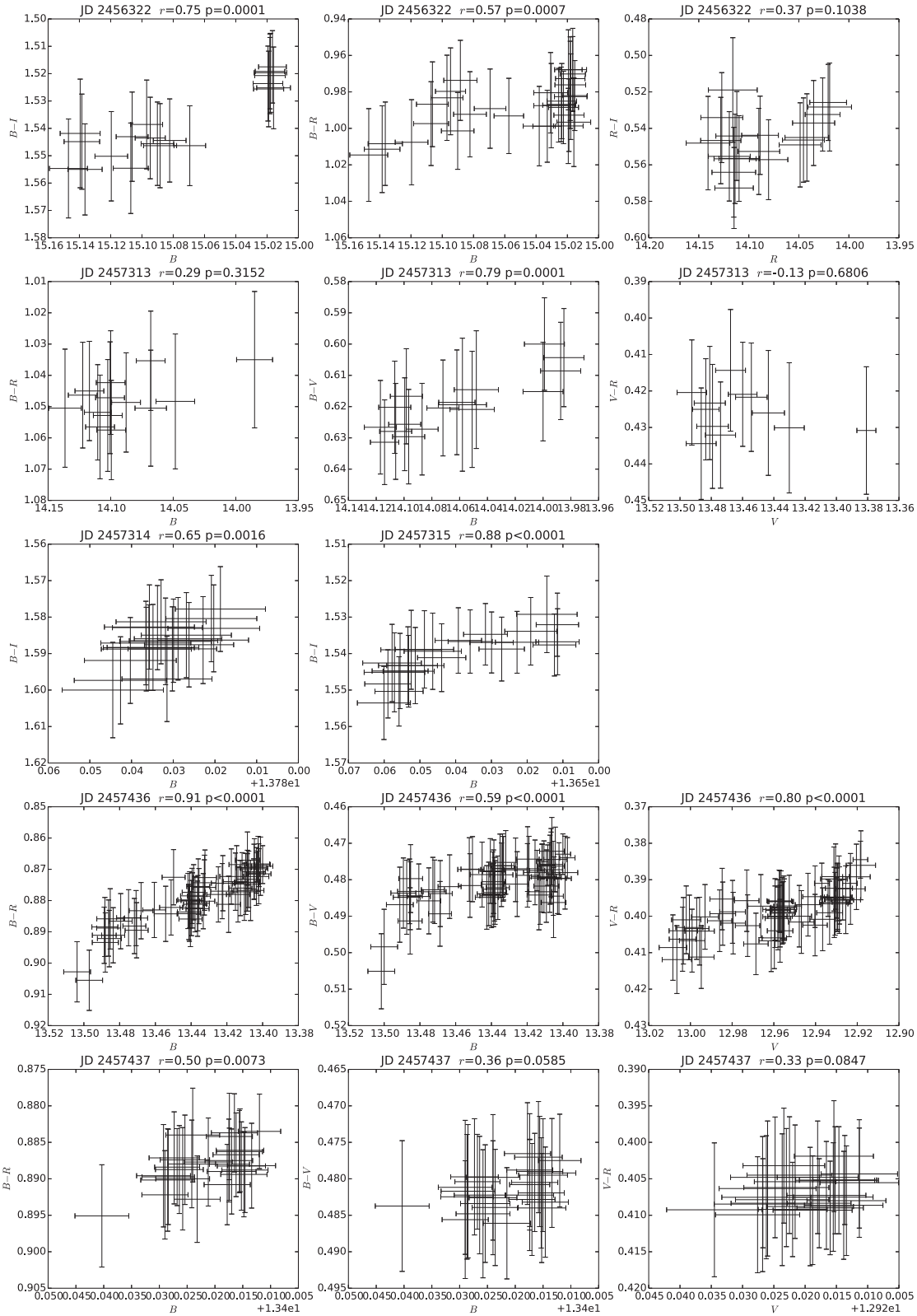

Figure 6. Colour–magnitude diagrams of 8-min binned light curves.

b. We ascribe them to the marginal variations of the check star. Considering that the light curves of the object pass both tests, we regard the object as variable. In additional to these abnormal events, on JD 245 7314, the light curve in the *B* band fails to pass the enhanced *F*-test but passes the nested ANOVA, indicating that the IDV is only beyond the limit of photometric accuracy. The object was probably variable on that night. In conclusion, the object was variable on all seven nights.

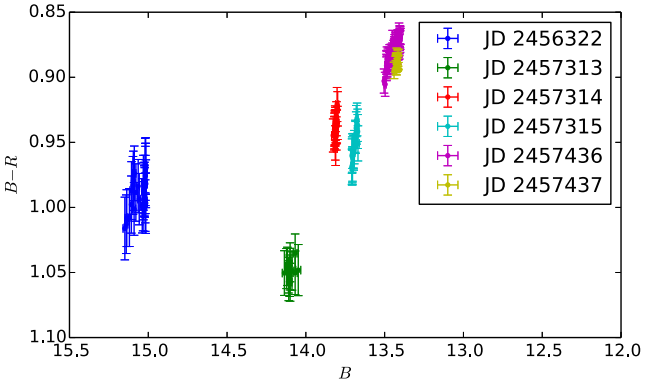

Figure 7. Long term colour–magnitude diagram between the *B* and *R* bands. Different colours indicate colour behaviours on different days.

3.3 Colour variations

To investigate the relationship between spectral changes and flux variations, we first calculate 8-min binned light curves and colours, and then plot the colour–magnitude diagrams. The results are shown in Fig. 6. The *R*-band light curves on JDs 245 7312, 245 7314 and 245 7315 are excluded. We also calculate the Spearman correlation coefficient and the associated p-value for each diagram. On JD 245 6322, the p-value of $B - I$ versus I on JD 245 6322 reaches 0.0001, indicating a mild bluer-when-brighter (BWB) colour behaviour. On JD 245 7436, the p-values of three diagrams are less than 0.0001, indicating a significant BWB trend. On JD 245 7313, the source shows almost no colour variation. Though the p-value of $B - V$ reaches 0.0001, it could be caused by the slight systematic bias between the 85 cm and 80 cm telescopes, because the colour index $B - R$ shows no variability. On JDs 245 7314 and 245 7437, the magnitude variations are too weak to show any colour variation. On JD 245 7315, the source showed an overall BWB trend but became achromatic at the bright end. The p-value confirms the colour variation.

We also plot the overall colour–magnitude diagram of the *B* and *R* bands in Fig. 7. The inter-day colour behaviour does not follow an overall BWB trend. The colour index $B - R$ shifted ∼0.1 mag from JDs 245 7313 to 245 7314. Though the *R*-band data of 2013 and 2015 are obtained with the 80 cm telescope with additional uncertainties, the 0.1-mag inter-day colour variation is far beyond the instrumental uncertainties. If we take the average value of the colour index from JDs 245 7313 to 245 7315, the long-term colour behaviour follows a mild BWB trend.

For different blazars, two distinct behaviours have been observed, i.e. redder-when-brighter (RWB) and BWB. The RWB behaviour appears mostly in FSRQs, while BL Lac objects exhibit more BWB events. On a timescale from months to years, for example, two of three FSRQs show RWB and three of four BL Lac objects show BWB in Gu et al. (2006)'s work. Four of six FSRQs are RWB and three of six BL Lac objects are BWB, as reported by Rani et al. (2010a). Eight of nine FSRQs are RWB in the SMARTS campaign (Bonning et al. 2012). In the monitoring by Ikejiri et al. (2011), three of seven FSRQs are RWB when they are in faint states while 23 of 27 BL Lac objects exhibit BWB behaviour.

Most reported that BWB chromatism of S5 0716+714 is on a short timescale (Ghisellini et al. 1997; Raiteri et al. 2003; Wu et al. 2012; Dai et al. 2013; Hu et al. 2014). However, Stalin et al. (2006) and Poon et al. (2009) found no clear evidence of intra-day BWB behaviour. Our intra-day results are consistent with most historical observations. On the long timescale, this BWB chromatism turns meagre, i.e. the long-term colour index versus magnitude slope is smaller than the short-term one (e.g. Wu et al. 2007). Our overall colour behaviour shows this trend as well. Raiteri et al. (2003) reported that the source tends to be achromatic on a 10-yr timescale. Our results are broadly consistent with the historical observation data.

3.4 Cross-correlation analysis

To investigate the inter-band time lags, we perform cross-correlation analysis. There are a couple of mathematical cross-correlation functions (CCF) and methods to detect lags and estimate the uncertainties. We adopt two sets of them.

The *z*-transformed discrete correlation function (ZDCF), introduced by Alexander (1997), corrects several biases of the discrete correlation function (DCF) (Edelson & Krolik 1988) by using equal population binning and Fisher's *z*-transform. Alexander (2013) offered a Fortran program, PLIKE, to calculate the ZDCF peak location based on the maximum likelihood (ML) estimation. The likelihood value of the *i*th point on the ZDCF curve, L_i, is approximately the probability that the correlation coefficient of this point is larger than that of any other ZDCF points. Hence, the maximum likelihood value is at the highest ZDCF point. The uncertainty of the lag is defined as the 68.2 per cent fiducial interval of the normalized likelihood function.

Another set of methods is proposed by Peterson et al. (1998, 2004), who employ a Monte Carlo (MC) method to estimate the peak position $\tau_{\rm peak}$ or the centroid position $\tau_{\rm cent}$ of an interpolated cross-correlation function (ICCF) and their uncertainties. In each MC realization, both 'flux randomization' (FR) and 'random subset selection' (RSS) processes are applied. The peak position $\tau_{\rm peak}$ and intensity $r_{\rm max}$ are obtained directly from the ICCF curve, and $\tau_{\rm cent}$ is calculated by points above a threshold, which is typically $0.8r_{\rm max}$. After a large number of MC realizations, distributions of the cross-correlation centroid (CCCD) and cross-correlation peak (CCPD) are built. The value of $\tau/\tau_{\rm peak}$ and its uncertainty are derived from the mean and the 1σ deviation of CCCD/CCPD. If the CCCD/CCPD is asymmetric, the lower and upper uncertainties are defined as values that correspond to 15.87 per cent and 84.13 per cent of the cumulative distribution function of CCCD/CCPD, respectively. For a broad ICCF peak, Peterson et al. (1998) recommended using $\tau_{\rm cent}$ rather than $\tau_{\rm peak}$.

The ZDCF and ICCF curves are plotted in Fig. 8. The *R*-band light curves on JDs 245 7412, 245 7414 and 245 7415 are excluded for cross-correlation analysis. On JD 245 6322, the curves of two CCFs are almost the same. Because of the vacancy interval on the *I*-band light curve, the left-hand sides of the peaks of *B* versus *I* and *R* versus *I* are flat. We adjust the threshold for centroid position estimation to a higher level properly. On JD 245 7313, significant deviations between the ZDCF and ICCF curves can be seen. Due to bad weather conditions that night, we clip data points with large photometric errors (see Section 2.2). The refined light curves have several significant gaps. Because ZDCF and ICCF have different strategies of sample collecting for correlation calculation, these unevenly sampled light curves could cause the deviations. On JD 245 7314, the low variation amplitude gives CCF curves with low correlation-coefficient values, which are lower than the threshold for the FR/RSS method. On JDs 245 7315, 245 7436 and 245 7437, the CCF curves show a significant symmetric peak.

We perform ML estimation for the ZDCF peak position and 5000 FR/RSS processes for the ICCF peak centroid estimation. The re-

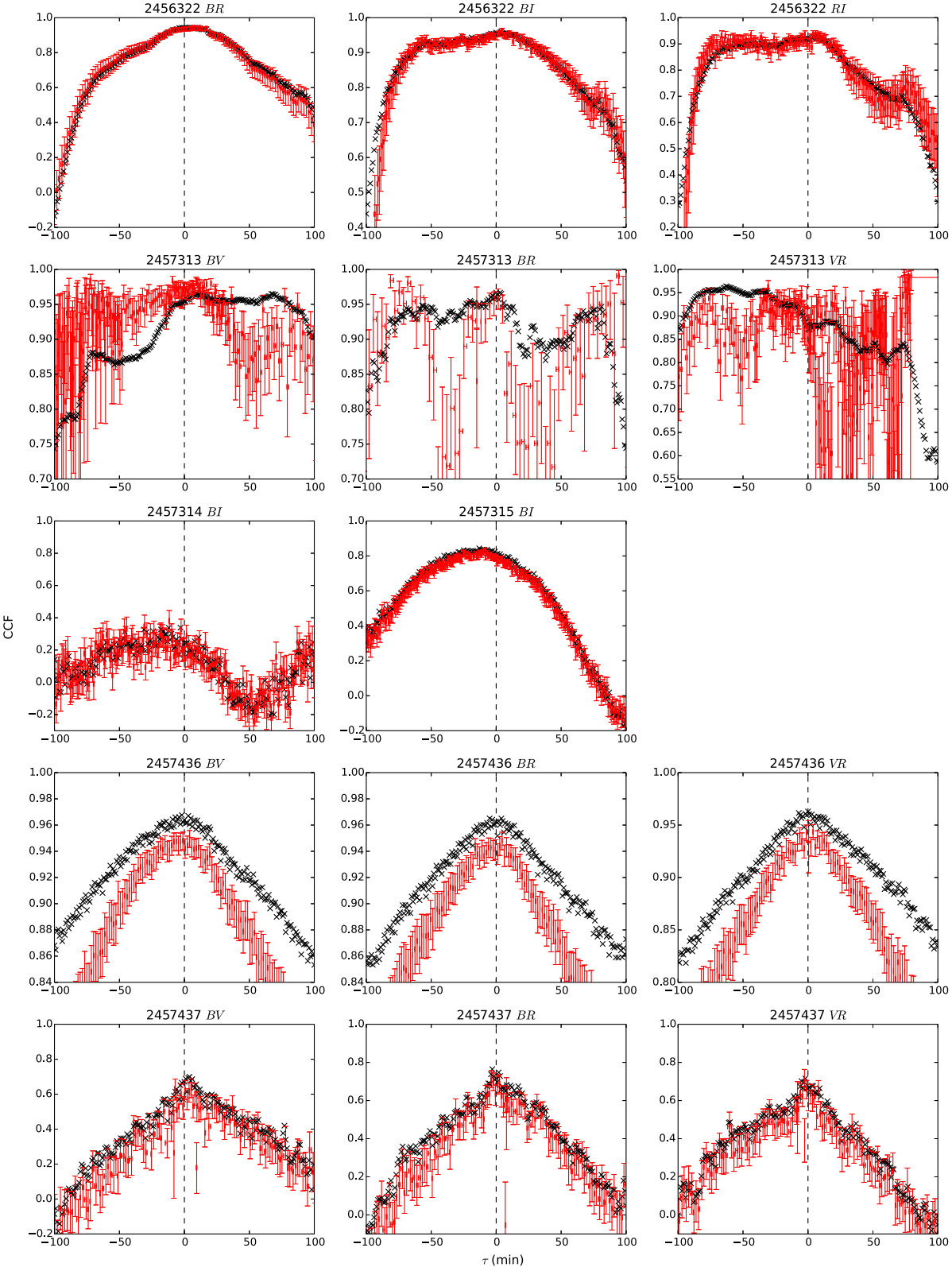

Figure 8. Results of the cross-correlation analysis. The black and red points are the ICCF and ZDCF curves, respectively. The black dashed lines indicate zero lags.

sults of the estimated time lags of the two methods as well as their CCF values at peak positions are listed in Table 4. On JD 245 6322, positive results estimated by the ZDCF/ML method indicate that variation in the *B* band leads that in the *R* and *I* bands, but no lag is detected by using the FR/RSS method. On JD 245 7315, variations in the *B* band lagged behind those in the *I* band by $8.7^{+6.9}_{-2.1}$

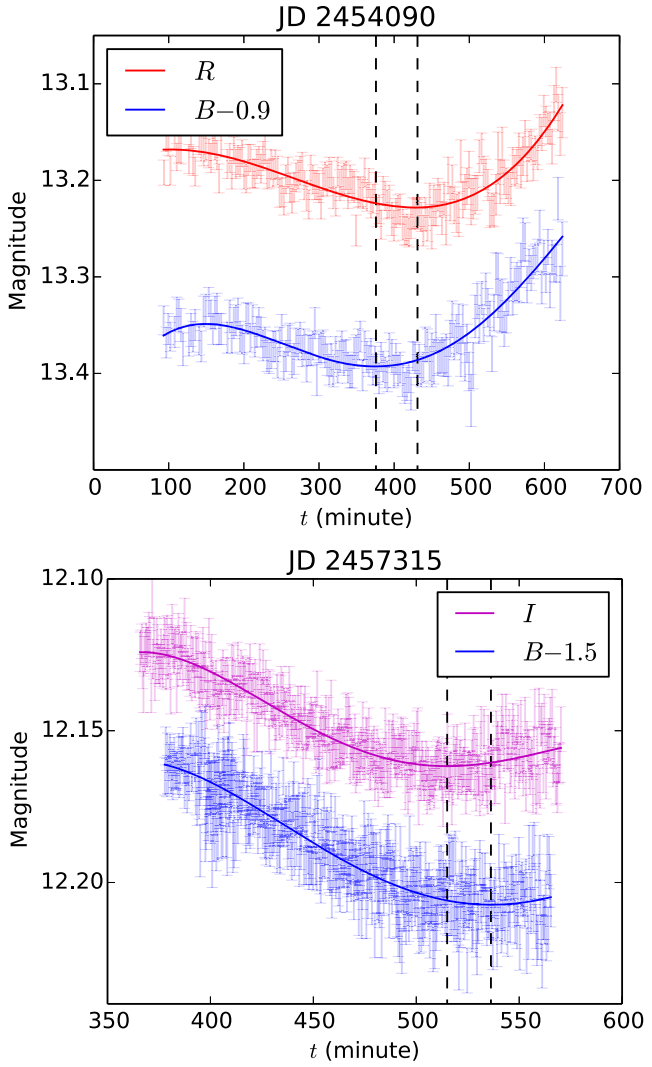

Figure 9. Top panel: polynomial fittings for the light curves in the *B* and *I* bands on JD 245 7315. The *B*-band light curve is shifted. Black dashed lines are the positions of the minima in the two light curves. Lower panel: the same as the top panel for the light curves on JD 245 4090 observed by Wu12.

min with the ZDCF/ML method and by 16.5 ± 3.1 min with the FR/RSS method. The zero point is out of the 1σ intervals of the two methods, and even out of the 3σ confidence interval calculated by the ICCF+FR/RSS method, which is 6.1–25.9 min. The estimated lags by the two methods are somewhat different; this is caused by the different estimation approaches. The ZDCF-ML method only considers the position of the maximum CCF value as the lag; if the maximum CCF point is not at the centroid, the fiducial distribution of likelihood can be skewed, which leads to an asymmetric uncertainty interval. On JD 245 7315, the maximum ZDCF point is on the right-hand side of the centroid. For this kind of broad CCF peak, the FR/RSS method for centroid estimation is more appropriate. The ZDCF/ML method, though having some deviation, proves the lag and constrains the lag value.

We perform fourth-order polynomial fittings for the light curves and calculate the minimum positions; see the upper panel of Fig. 9. The ∼20-min lag between the two minima is close to the results of the cross-correlation. We compare this result with the lag on JD 245 4090 observed by Wu et al. (2012, hereafter Wu12) (lower panel of Fig. 9). There are a couple of similarities between these two lags: the values of the delays are both of tens of minutes; they are both at the junctions of two flares; at least one flare follows the BWB chromatism. The difference is that the variation in the long wavelength leads that at the short wavelength on JD 245 7315, while the result on JD 245 4090 is the reverse.

4 DISCUSSION

During our multi-band observation, mild BWB colour behaviours and one inter-band time lag were observed.

Several models can interpret the BWB chromatism. Within a one-component synchrotron model, a flatter spectrum or a lower spectral index at the high state indicates a flatter relativistic electron spectrum. When the source gets brighter, more electrons are accelerated by the shock and injected into the emission region (Fiorucci, Ciprini & Tosti 2004). The BWB trend can be interpreted by a two-component model as well, which includes an underlying component on the red side and a broad-band achromatic variable synchrotron component, especially when the source is faint (Wierzcholska et al. 2015). This underlying component could be from the host galaxy, whose SED peak is located at near-infrared frequencies. However, for S5 0716+714, the magnitude of the host galaxy is only 17.5 in the *I* band (Nilsson et al. 2008). Such a faint host galaxy only contributes less than 0.02 mag of $B - I$ colour variation when the source turns bright from 13.5 to 13.3 mag in the *I* band. This contribution could somehow lead to a marginal BWB trend at a dim state, as in the case of the $B - I$ colour behaviour on JD 245 6322, but cannot explain significant colour variabilities at high states (e.g. Wu et al. 2005). Another interpretation is synchrotron-peak shift. Since the synchrotron peak of S5 0716+714 is located at near-IR to UV frequencies, the optical colour index should be sensitive to the peak shifts. Liao et al. (2014) reported that the $\nu_{\rm syn\_peak}$ exceeded the *V* band when the source was in a bright state. The peak shift could be caused either by high-energy electron injection or by variation of the Doppler factor δ (Ikejiri et al. 2011). However the factor of δ variation might be ruled out, because the Doppler factor amplifies the emission coefficient by three orders of magnitude but only one for the observational frequency. Raiteri et al. (2003) explain the long-term variation of this source by a variation of $\delta \sim 1.3$. Such a subtle change only accounts for achromatic behaviours.

Inter-band time lags indicate unconformities of variations at different wavelengths, or the so-called spectral hysteresis. Previous spectral hysteresis studies focused on the whole profile of flares (e.g. Fossati et al. 2000a; Zhang et al. 1999). Injection and acceleration of relativistic electrons into the radiation zone and the subsequent radiative-cooling process can account for the observed phenomena (Kirk, Rieger & Mastichiadis 1998). However, we only observed a time lag between the minima of two light curves in different bands. We propose a possibility to produce such lags at trough positions. The left-hand part of the bottom on JD 245 7315 and the right-hand part on JD 245 4090 are mildly BWB with the opposition parts nearly achromatic. The nearly achromatic variation changes the timescales of previous/subsequent BWB variations at different wavelengths. Variation in the long-wavelength band has a shorter timescale than that of the short-wavelength band. This could explain why the variations in the long-wavelength band lead those in the short-wavelength band on JD 245 7315, but lagged on JD 245 4090.

In general, this kind of 'lag' could appear at troughs where the adjacent flares have different colour behaviours. It raises another question: why have we only observed a small number of them?

Table 3. Results of the IDV test.

Julian date	Filter	Enhanced F-test				Nested ANOVA for blazar				Nested ANOVA for star 5				Variable
		F	ν_1	ν_2	P	F	ν_1	ν_2	P	F	ν_1	ν_2	P	
245 6322	*B*	29.06	229	1374	<0.0001	61.81	45	184	<0.0001	1.06	45	184	0.3830	V
	I	16.83	423	2538	<0.0001	74.64	83	336	<0.0001	6.17	83	336	<0.0001[b]	V
	R	9.75	128	768	<0.0001	152.59	24	100	<0.0001	23.49	24	100	<0.0001[a]	V
245 7312	*I*	2.97	266	1596	<0.0001	18.94	52	212	<0.0001	1.81	52	212	0.0018	V
	R	1.84	228	1368	<0.0001	20.93	44	180	<0.0001	6.55	44	180	<0.0001[a]	V
245 7313	*B*	13.96	43	258	<0.0001	102.30	7	32	<0.0001	4.26	7	32	0.0020	V
	R	9.80	38	228	<0.0001	28.02	6	28	<0.0001	2.82	6	28	0.0029	V
	V	13.28	616	3696	<0.0001	98.74	122	492	<0.0001	1.09	122	492	0.2557	V
245 7314	*B*	1.16	271	1626	0.0512	2.22	53	216	<0.0001	1.33	53	216	0.0838	P
	I	1.71	212	1272	<0.0001	5.77	41	168	<0.0001	1.14	41	168	0.2815	V
	R	0.79	199	1194	0.9818[a]	15.97	39	160	<0.0001	4.46	39	160	<0.0001[a]	
245 7315	*B*	2.89	476	2856	<0.0001	17.65	94	380	<0.0001	0.77	94	380	0.9352	V
	I	5.45	482	2892	<0.0001	26.66	95	384	<0.0001	1.16	95	384	0.1708	V
	R	0.63	231	1386	1.0000[a]	10.48	45	184	<0.0001	4.31	45	184	<0.0001[a]	
245 7436	*B*	22.41	289	1734	<0.0001	179.57	57	232	<0.0001	4.72	57	232	<0.0001[b]	V
	R	7.18	290	1740	<0.0001	121.56	57	232	<0.0001	3.11	57	232	<0.0001[b]	V
	V	12.26	286	1716	<0.0001	111.60	56	228	<0.0001	2.53	56	228	<0.0001[b]	V
245 7437	*B*	1.89	130	780	<0.0001	12.00	25	104	<0.0001	0.97	25	104	0.5106	V
	R	1.60	133	798	<0.0001	8.27	25	104	<0.0001	1.28	25	104	0.1966	V
	V	1.87	152	912	<0.0001	9.29	29	120	<0.0001	1.74	29	120	0.0202	V

[a]Caused by unknown interference in the light path of the 80 cm telescope.
[b]Caused by marginal variation of the check star.

Table 4. Results of the cross-correlation analysis. Positive values indicate that the previous band leads the latter band.

JD	Passbands	ZDCF-ML		ICCF-FR/RSS	
		Lag (min)	$\mathrm{ZDCF_{peak}}$	Lag (min)	$\mathrm{ICCF_{peak}}$
245 6322	$B-R$	$10.6^{+4.8}_{-7.5}$	0.94	4.0 ± 5.8	0.94
	$B-I$	$4.6^{+5.2}_{-2.5}$	0.96	1.3 ± 6.9	0.96
	$R-I$	$5.9^{+3.7}_{-40.1}$	0.94	− 7.9 ± 18.0	0.93
245 7313	$B-V$	$-8.9^{+18.9}_{-4.1}$	0.98	− 5.5 ± 9.6	0.96
	$B-R$	$1.6^{+2.5}_{-9.2}$	0.96	− 2.7 ± 36.8	0.97
	$V-R$	$-30.5^{+24.8}_{-2.3}$	0.96	− 9.7 ± 17.7	0.96
245 7314	$B-I$	$-11.6^{+8.7}_{-27.8}$	0.38	–	0.32
245 7315	$B-I$	$-8.7^{+2.1}_{-6.9}$	0.83	− 16.5 ± 3.1	0.84
234 7436	$B-V$	$4.0^{+4.6}_{-11.8}$	0.95	− 2.9 ± 5.4	0.97
	$B-R$	$4.5^{+3.6}_{-10.6}$	0.94	− 4.3 ± 6.0	0.97
	$V-R$	$0.5^{+6.8}_{-4.2}$	0.94	− 0.2 ± 5.2	0.96
245 7437	$B-V$	$5.2^{+3.6}_{-7.9}$	0.64	6.9 ± 13.9	0.70
	$B-R$	$-3.7^{+5.4}_{-1.1}$	0.71	− 0.9 ± 1.8	0.76
	$V-R$	$-2.7^{+8.3}_{-1.9}$	0.71	− 3.4 ± 13.1	0.68

Four main parameters that determine the lag detection have been discussed by Wu12; they are wavelength separation, variation amplitude, temporal resolution and measurement accuracy. Furthermore, the cross-correlation analysis is always applied to the whole light curve instead of the trough part. If the light curve has other features, lags at troughs could be offset.

5 CONCLUSION

We monitored the BL Lac object S5 0716+714 on seven nights from 2013 to 2016. Several telescopes were utilized for multi-colour quasi-simultaneous observations with high temporal resolution. The main results of our observation are as follows:

(i) We used two statistical methods and IDV was detected on all seven nights.

(ii) During our observations, the object became brightest (R = 12.51) on JD 245 7437 and faintest (R = 14.15) on JD 245 6322. The maximum intra-day variation was 0.15 mag in the R band.

(iii) Achromatic and mild BWB intra-day spectral behaviours were observed. In the long term, the colour variation does not follow the BWB trend strictly.

(iv) On JD 245 7315, a ∼15-15-min inter-band lag was detected by two independent methods.

(v) We compare the lag with that of Wu12, and propose a hypothesis that these kinds of inter-band lags at troughs between two flares could be produced due to the inconsistency of variation timescales at different wavelengths.

ACKNOWLEDGEMENTS

We thank the referee for important comments and constructive suggestions for improving our manuscript. This work has been supported by the National Natural Science Foundation of China grants U1531242.

REFERENCES

Abdo A. A. et al., 2010, ApJ, 716, 30
Agarwal A. et al., 2016, MNRAS, 455, 680
Alexander T., 1997, in Maoz D., Sternberg A., Leibowitz E. M., eds, Astrophysics and Space Science Library Vol. 218, Astronomical Time Series, Springer Netherlands. p. 163https://www.springer.com/gp/book/9780792347064
Alexander T., 2013, preprint (arXiv:1302.1508)
Bachev R., Strigachev A., Semkov E., 2005, MNRAS, 358, 774
Bhatta G. et al., 2013, A&A, 558, A92
Bhatta G. et al., 2016, ApJ, 831, 92
Bonning E. et al., 2012, ApJ, 756, 13
Böttcher M., Dermer C. D., 2010, ApJ, 711, 445
Böttcher M. et al., 2003, ApJ, 596, 847
Carini M. T., Walters R., Hopper L., 2011, AJ, 141, 49
Chiaberge M., Ghisellini G., 1999, MNRAS, 306, 551
Dai Y., Wu J., Zhu Z.-H., Zhou X., Ma J., Yuan Q., Wang L., 2013, ApJS, 204, 22
Danforth C. W., Nalewajko K., France K., Keeney B. A., 2013, ApJ, 764, 57
de Diego J. A., 2010, AJ, 139, 1269
de Diego J. A., Polednikova J., Bongiovanni A., Pérez García A. M., De Leo M. A., Verdugo T., Cepa J., 2015, AJ, 150, 44
Dermer C. D., 1998, ApJ, 501, L157
Edelson R. A., Krolik J. H., 1988, ApJ, 333, 646
Fiorucci M., Ciprini S., Tosti G., 2004, A&A, 419, 25
Fossati G. et al., 2000a, ApJ, 541, 153
Fossati G. et al., 2000b, ApJ, 541, 166
Garcia A., Sodré L., Jablonski F. J., Terlevich R. J., 1999, MNRAS, 309, 803
Gaur H., Gupta A. C., Wiita P. J., 2012a, AJ, 143, 23
Gaur H. et al., 2012b, MNRAS, 420, 3147
Gaur H. et al., 2012c, MNRAS, 425, 3002
Ghisellini G. et al., 1997, A&A, 327, 61
Gopal-Krishna Stalin C. S., Sagar R., Wiita P. J., 2003, ApJ, 586, L25
Goyal A., Mhaskey M., Gopal-Krishna Wiita P. J., Stalin C. S., Sagar R., 2013, JA&A, 34, 273
Gu M. F., Lee C.-U., Pak S., Yim H. S., Fletcher A. B., 2006, A&A, 450, 39
Gupta A., 2018, Galaxies, 6, 1
Gupta A. C., Fan J. H., Bai J. M., Wagner S. J., 2008, AJ, 135, 1384
Gupta A. C., Joshi U. C., 2005, A&A, 440, 855
Heidt J., Wagner S. J., 1996, A&A, 305, 42
Hong S., Xiong D., Bai J., 2017, AJ, 154, 42
Hong S., Xiong D., Bai J., 2018, AJ, 155, 31
Howell S. B., Mitchell K. J., Warnock A.,, III, 1988, AJ, 95, 247
Hu S. M., Chen X., Guo D. F., Jiang Y. G., Li K., 2014, MNRAS, 443, 2940
Ikejiri Y. et al., 2011, PASJ, 63, 639
Kataoka J., Takahashi T., Makino F., Inoue S., Madejski G. M., Tashiro M., Urry C. M., Kubo H., 2000, ApJ, 528, 243
Kirk J. G., Rieger F. M., Mastichiadis A., 1998, A&A, 333, 452
Liao N. H., Bai J. M., Liu H. T., Weng S. S., Chen L., Li F., 2014, ApJ, 783, 83
Liu X. et al., 2017, MNRAS, 469, 2457
Man Z., Zhang X., Wu J., Yuan Q., 2016, MNRAS, 456, 3168
Miller H. R., Carini M. T., Goodrich B. D., 1989, Nature, 337, 627
Montagni F., Maselli A., Massaro E., Nesci R., Sclavi S., Maesano M., 2006, A&A, 451, 435
Nesci R., Massaro E., Rossi C., Sclavi S., Maesano M., Montagni F., 2005, AJ, 130, 1466
Nilsson K., Pursimo T., Sillanpää A., Takalo L. O., Lindfors E., 2008, A&A, 487, L29
Peterson B. M., Wanders I., Horne K., Collier S., Alexander T., Kaspi S., Maoz D., 1998, PASP, 110, 660
Peterson B. M. et al., 2004, ApJ, 613, 682
Poon H., Fan J. H., Fu J. N., 2009, ApJS, 185, 511
Qian B., Tao J., Fan J., 2000, PASJ, 52, 1075
Raiteri C. M. et al., 2003, A&A, 402, 151
Raiteri C. M. et al., 2008, A&A, 491, 755
Rani B., Gupta A. C., Joshi U. C., Ganesh S., Wiita P. J., 2010b, ApJ, 719, L153
Rani B. et al., 2010a, MNRAS, 404, 1992
Rani B. et al., 2013, A&A, 552, A11
Spada M., Ghisellini G., Lazzati D., Celotti A., 2001, MNRAS, 325, 1559
Stalin C. S., Gopal-Krishna Sagar R., Wiita P. J., 2004, MNRAS, 350, 175
Stalin C. S., Gopal-Krishna Sagar R., Wiita P. J., Mohan V., Pandey A. K., 2006, MNRAS, 366, 1337
Takahashi T. et al., 1996, ApJ, 470, L89
Urry C. M., Padovani P., 1995, PASP, 107, 803
Villata M., Raiteri C. M., Lanteri L., Sobrito G., Cavallone M., 1998, A&AS, 130, 305
Villata M. et al., 2000, A&A, 363, 108
Villata M. et al., 2008, A&A, 481, L79
Villata M. et al., 2009, A&A, 501, 455
Wagner S. J. et al., 1996, AJ, 111, 2187
Wierzcholska A., Ostrowski M., Stawarz Ł., Wagner S., Hauser M., 2015, A&A, 573, A69
Wu J., Böttcher M., Zhou X., He X., Ma J., Jiang Z., 2012, AJ, 143, 108
Wu J., Peng B., Zhou X., Ma J., Jiang Z., Chen J., 2005, AJ, 129, 1818
Wu J., Zhou X., Ma J., Wu Z., Jiang Z., Chen J., 2007, AJ, 133, 1599
Zhang Y. H. et al., 1999, ApJ, 527, 719

This paper has been typeset from a TEX/LATEX file prepared by the author.